J. Fluid Mech. (2021), *vol*. 920, A10, doi:10.1017/jfm.2021.434

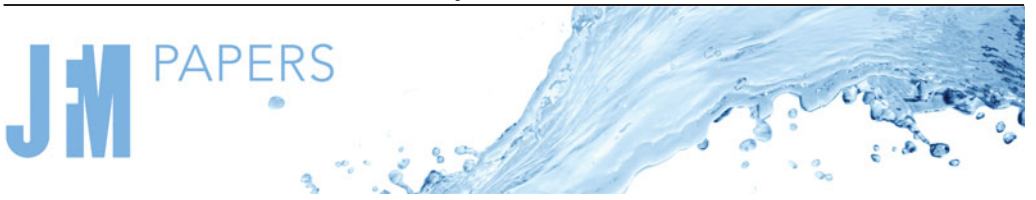

Estimating thrust from shedding vortex surfaces in the wake of a flapping plate

Wenwen Tong[1], **Yue Yang**[1,2,†] **and Shizhao Wang**[3,4]

[1]State Key Laboratory for Turbulence and Complex Systems, College of Engineering, Peking University, Beijing 100871, PR China

[2]CAPT and BIC-ESAT, Peking University, Beijing 100871, PR China

[3]LNM, Institute of Mechanics, Chinese Academy of Sciences, Beijing 100190, PR China

[4]School of Engineering Sciences, University of Chinese Academy of Sciences, Beijing 100049, PR China

(Received 5 January 2021; revised 9 April 2021; accepted 16 May 2021)

We elucidate the vortex dynamics of flows past a flapping plate using the vortex-surface field (VSF) and develop models for estimating thrust from shedding vortex surfaces in wakes. The VSF evolution is calculated from numerical simulation using the immersed boundary method. The VSF visualization reveals that a spoon-like vortex surface dominated by tip vortex lines is formed and periodically shed into the wake owing to the alternating upstroke and downstroke of the flapping plate. We simplify the finite-domain impulse theory based on a particular vortex surface. The simplified theory demonstrates that the force on the plate is only dependent on the vortical impulse and Lamb-vector integral of the vortex surface enclosing the plate. Then, we propose a time-averaged thrust model from near-wake discrete vortex surfaces, where the incorporation of the Lamb-vector integral significantly improves the model estimation from the impulse model. Furthermore, we estimate the mean thrust based on two arbitrary vortex surfaces in the far wake from the linear impulse decay of periodically shedding vortex surfaces, which provides a possible approach to infer the state of the moving body in experimental investigation and practical applications.

Key words: vortex dynamics, propulsion, swimming/flying

1. Introduction

The wake of biological locomotion (Dabiri 2009; Shyy *et al.* 2010; Wu 2011; Phan & Park 2019) and aerial/underwater vehicles (Jiménez, Hultmark & Smits 2010; Park *et al.* 2014; Bhat *et al.* 2020), similar to the footprint, can reveal rich physical information of the moving body. In particular, the shedding vortical structures propagate downstream in

† Email address for correspondence: yyg@pku.edu.cn

the far wake with measurable velocity and vorticity fields, e.g. in the wake of a flying bird (Hubel *et al.* 2010) or swimming fish (Lauder 2015; Mendelson & Techet 2015). These structures can be utilized to infer the forces exerted on the moving body.

The experimental measurement of biological locomotion in the far wake is more feasible than the near-wall measurement of forces owing to the complex boundary condition of the moving body. Thus, the shedding vortical structures in the wake have been extensively investigated in experiments and numerical simulations (e.g. Lauder & Drucker 2002; Spedding, Rosén & Hedenström 2003; Dong, Mittal & Najjar 2006; King, Kumar & Green 2018; Chen *et al.* 2020; Oh *et al.* 2020). To mimic the wing/fin motion of a flying animal/swimming fish, the flapping plate is a useful model problem to study the vortex dynamics in wake structures (e.g. Li & Lu 2012; Buchner, Honnery & Soria 2017; Wang, He & Liu 2019).

The ring-like vortical structures have been widely observed in the wake of the flapping plate or foil and used as a simple vortex model to estimate forces on the moving body (see Blondeaux *et al.* 2005; Buchholz & Smits 2006, 2008; Li & Dong 2016). For a flapping foil with a low aspect ratio, Dong *et al.* (2006) numerically investigated the wake topology to understand the hydrodynamic performance of fish fins. They found that the wake is dominated by two sets of ring-like vortical structures during periodical flapping motion, and these structures evolve into vortex rings as they propagate downstream. Dabiri (2009) explained the vortex formation process related to the propulsion in biological and bio-inspired systems. For the flapping plate with a large aspect ratio, the wake topology is represented by interconnected vortical structures (Wang, He & Zhang 2015), and the geometry of the vortical structures can be very convoluted in biological locomotion such as birds and bats (Hedenström, Rosén & Spedding 2006; Hedenström *et al.* 2007).

The wake information can be utilized to estimate forces owing to the momentum transfer from the moving body to the fluid (see Drucker & Lauder 1999; Lauder & Drucker 2002; Spedding *et al.* 2003; Lee *et al.* 2013; Park *et al.* 2016). If a wake can be represented by distinct closed-loop and discrete vortices, forces were directly estimated through the vortical impulse of a discrete vortex. Lauder & Drucker (2002) simplified wake structures near the moving body as vortex rings and calculated the time-averaged thrust using the vortical impulse during the flapping cycle. The vortical impulse of vortex rings is calculated through the spanwise vorticity on the spanwise symmetry plane (Müeller *et al.* 1997; Gharib, Rambod & Shariff 1998), and has been used to estimate the thrust from the wake (Li & Lu 2012). Dabiri (2005) incorporated the vortex-added-mass force into the vortex-ring model to improve the force estimation. On the other hand, if the shape of vortical structure is very different from a ring, the over-simplification of vortex rings can introduce a large discrepancy into the force estimation (Lauder 2015).

Compared with the simple vortex-ring model under phenomenological assumptions, a general theory of aerodynamic forces has been developed to reveal the relationship between the forces on the moving body and local vortex dynamics (see Wu, Ma & Zhou 2015). From the structure level, Wu, Liu & Liu (2018) summarized the vortex-force theory and impulse theory for calculating forces from local vortical structures with derivative-moment transformations. Moreover, Chang (1992) developed the force-element theory based on potential flows, which was applied to analyse the forces on an impulsively started finite plate (Lee *et al.* 2012) and a heaving plate (Lin *et al.* 2018).

In the classical vortex-force theory (Prandtl 1918) in inviscid incompressible flow, the force can be solely determined by the Lamb vector, sometimes referred to as the vortex force. Wu, Lu & Zhuang (2007) developed the unsteady vortex-force theory to indicate that the force exerted on the moving body is dominated by the vortex force. Wang *et al.* (2019) proposed the wake-sectional Kutta–Joukowski model to estimate lift based on the

vortex-force theory from the wake velocity data on the Trefftz plane for complex wake structures in flapping flight.

In the impulse theory (Wu 1981; Lighthill 1986), the force acting on the body is directly related to the change of the fluid impulse (Burgers 1920), so the impulse theory can be used to estimate forces from wake vortical structures. Birch & Dickinson (2003) investigated the influence of wing–wake interactions on aerodynamic forces in flapping flight based on the time derivative of the vortical impulse. Wang & Wu (2010) identified the role of vortex rings and their mutual interactions in force production/reduction for a flapping flight using the vorticity moment of wake structures.

The general impulse theory with an arbitrary integral domain was proposed by Noca, Shiels & Jeon (1997, 1999) to evaluate time-dependent aerodynamic forces on the body. Kang *et al.* (2018) developed the minimum-domain impulse theory to minimize the integral domain to calculate unsteady aerodynamic forces, indicating that the force exerted on the moving body is dominated by vortical structures connecting to the body (Li & Lu 2012). The criterion for splitting the minimum domain, however, is very strict, hindering the application of the minimum-domain impulse theory to three-dimensional flows. Furthermore, the impulse was calculated from the vortical structure enclosing the moving body in previous studies, so its practical value is limited compared with the direct calculation of forces from the body boundary. Hence, it is necessary to extend the impulse theory to estimate forces from shedding vortical structures in the far wake for applications.

For structure-based force estimation, the identification and segmentation of vortical structures are crucial for the accuracy and applicability. Eulerian vortex identification methods (e.g. Hunt, Wray & Moin 1988; Jeong & Hussain 1995) based on the local velocity gradient were usually applied to identify vortical structures, but they cannot ensure the time coherence in the tracking of a particular vortical structure and they have no explicit link to the vorticity-based, vortex-force/impulse theories. Yang & Pullin (2010) developed the vortex-surface field (VSF), a Lagrangian-based identification method, and the VSF has been applied to various flows to elucidate the vortex dynamics (e.g. Zhao, Yang & Chen 2016; Xiong & Yang 2019) and develop structure-based force models (Zheng *et al.* 2019) from a Lagrangian-like view. In particular, Tong, Yang & Wang (2020) applied the VSF to the flow past a stationary finite plate to characterize three-dimensional features of vortex surfaces. Additionally, the modal decomposition can extract dominant modes in the flow field (Taira *et al.* 2017), and proper orthogonal decomposition was applied to analyse forces based on the dominant modes for a low-aspect-ratio plate (Li, Dong & Liang 2016).

In the present study, we extend the VSF to flows past a flapping plate to elucidate vortex generation and shedding mechanisms. Then, we simplify the finite-domain impulse theory based on a particular vortex surface, and develop models to infer thrust from shedding vortex surfaces in the far wake. The outline of this paper is as follows. In § 2, we describe the numerical implementation for calculating the velocity field and the VSF for flows past a flapping plate. In § 3, we elucidate the shedding mechanism of vortex surfaces. In § 4, we develop near-wake and far-wake models to estimate the thrust from the shedding vortex surfaces. Some conclusions are drawn in § 5.

2. Simulation overview

2.1. *Immersed boundary method*

We carry out the direct numerical simulation (DNS) of a three-dimensional uniform flow past a flapping plate with the free-stream velocity U. The zero-thickness plate heaves

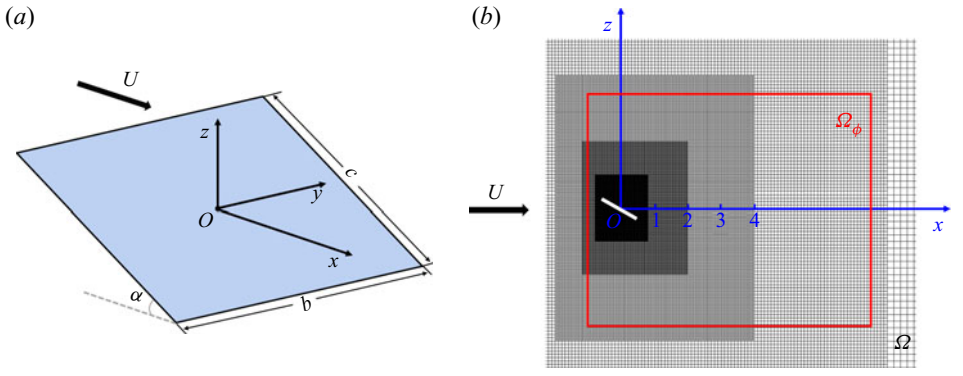

Figure 1. Schematic diagrams of the coordinate system and local-refined mesh. (*a*) Flow past a flapping plate with the coordinate system *O*-*xyz*. (*b*) Flow-field domain Ω and VSF domain Ω_ϕ on the x–z plane at $y = 0$. The white line denotes the plate, and the x-coordinate denotes the streamwise position non-dimensionalized by the chord length.

vertically and pitches around the centre of the plate. The plate has the chord length c and fixed wing span $b = R_A c$, where R_A is the aspect ratio. Figure 1(*a*) sketches the flapping plate and the Cartesian coordinate system with the x-axis along the streamwise direction, the y-axis along the spanwise direction and the z-axis along the vertical direction. The kinematics of the flapping plate is characterized by the angle of attack

$$\alpha(t) = \alpha_0 + \alpha_m \cos(2\pi f t), \tag{2.1}$$

and the vertical position of the plate centre

$$z_c(t) = z_{c0} + A \sin(2\pi f t), \tag{2.2}$$

where α_m and A respectively denote the pitching and heaving amplitudes, α_0 and z_{c0} respectively denote the time-averaged α and z_c, f is the flapping frequency and t is the physical time. All the variable and parameters in the present study are non-dimensionalized by U and c.

Motivated by the numerical simulations (Dong *et al.* 2006; Li & Lu 2012; Wang *et al.* 2013; Li & Dong 2016) and experiments (Buchholz & Smits 2006, 2008) of low-aspect-ratio flapping wings, we conduct a series of DNS cases with the varying parameters listed in table 1. Here, $Re = Uc/\nu$ is the Reynolds number with the kinematic viscosity ν, and $St = 2Af/U$ is the Strouhal number. Case 1 with $St = 0.6$ is mainly used to study of the VSF evolution and force modelling. This case has a discrete wake dominated by two sets of isolated vortical structures, similar to the wake topology observed in Dong *et al.* (2006), Li & Lu (2012), Li & Dong (2016) and Li *et al.* (2016). Furthermore, the wake can be more convoluted with the increase of Re, St or R_A (Dong *et al.* 2006; Wang *et al.* 2013; Liu, Dong & Li 2016).

The incompressible flow past a flapping plate is governed by the Navier–Stokes equations

$$\frac{\partial \boldsymbol{u}}{\partial t} + \boldsymbol{u} \cdot \nabla \boldsymbol{u} = -\nabla p + \frac{1}{Re}\nabla^2 \boldsymbol{u} + \boldsymbol{f}, \tag{2.3}$$

$$\nabla \cdot \boldsymbol{u} = 0, \tag{2.4}$$

where $\boldsymbol{u}$, p and $\boldsymbol{f}$ denote the non-dimensional velocity, pressure and body force, respectively. We use the immersed boundary method with the discrete streamfunction

Case	R_A	α_0	α_m	f	A	Re	St
1	1	0	30	0.6	0.5	200	0.6
2	1	10	30	0.6	0.5	200	0.6
3	1	0	30	0.5	0.5	200	0.5
4	1	0	30	0.6	0.5	300	0.6
5	2	0	30	0.6	0.5	200	0.6
6	1	0	30	0.8	0.5	200	0.8

Table 1. Parameters for the flapping plate in the DNS.

(Wang & Zhang 2011) to solve (2.3) and (2.4). The geometry and kinematics of the plate are described by Lagrangian marker points uniformly distributed on the immersed boundary. The interpolation and spreading of forces on Eulerian and Lagrangian points are linked by the regularized delta function δ_h (Peskin 2002) as

$$\sum_{j=1}^{M}\left(\sum_{\boldsymbol{x}}\delta_h(\boldsymbol{x}-\boldsymbol{X}_j)\delta_h(\boldsymbol{x}-\boldsymbol{X}_k)(\Delta s)^2(\Delta x)^3\right)\boldsymbol{F}(\boldsymbol{X}_j)=\frac{\boldsymbol{U}_b(\boldsymbol{X}_k)-\boldsymbol{U}^*(\boldsymbol{X}_k)}{\Delta t}, \tag{2.5}$$

and

$$\boldsymbol{f}(x)=\sum_{j=1}^{M}\boldsymbol{F}(\boldsymbol{X}_j)\delta_h(\boldsymbol{x}-\boldsymbol{X}_j)(\Delta s)^2, \tag{2.6}$$

where $\boldsymbol{x}$ and $\boldsymbol{X}$ are Eulerian and Lagrangian points, respectively, $\boldsymbol{f}$ and $\boldsymbol{F}$ are the forces on Eulerian and Lagrangian points, respectively, Δs and Δx are Lagrangian and Eulerian grid spacings, respectively, $\boldsymbol{U}_b$ and $\boldsymbol{U}^*$ are specified and predicted velocities at kth Lagrangian points, respectively, and M is the total number of Lagrangian points on the immersed boundary. The details and validation of our implementation of the immersed boundary method can be found in Wang & Zhang (2011) and Wang *et al.* (2013).

The thrust coefficient of the flapping plate is

$$C_T=\frac{F_T}{\frac{1}{2}\rho U^2 R_A c^2}, \tag{2.7}$$

where F_T is the thrust of the flapping plate. From the DNS data, it is calculated by

$$C_T=-\frac{\sum_{k=1}^{M}F_x(\boldsymbol{X}_k)(\Delta s)^2}{\frac{1}{2}\rho U^2 R_A c^2}, \tag{2.8}$$

where F_x denotes the x-component of the force on Lagrangian points.

As shown in figure 1(*b*), the present simulation is performed in a rectangular domain of $\Omega\in[-14,22]\times[-18,18]\times[-18,18]$. The uniform inflow velocity U is prescribed at the inlet and the fixed pressure condition is specified at the outlet. The slip-wall condition is used at the other four boundaries and the no-slip condition is specified on the plate. The initial condition for the flow is $\boldsymbol{u}=(U,0,0)$. A locally refined mesh with the minimum spacing $\Delta x=0.0125$ is applied around the immersed boundary to achieve the high spatial resolution near the plate, and the maximum spacing $\Delta x=0.4$ is applied in the far field to reduce the computational cost. The total number of grid points is 12 million.

The effectiveness of the present mesh spacing and computational domain has been validated by a convergence test via varying the grid size and computational domain in Appendix A.

2.2. *VSF method*

The VSF is a smooth scalar field satisfying the constraint (see Yang & Pullin 2010)

$$\boldsymbol{\omega} \cdot \boldsymbol{\nabla} \phi_v = 0, \tag{2.9}$$

where $\boldsymbol{\omega} = \boldsymbol{\nabla} \times \boldsymbol{u}$ is the vorticity, so that the isosurface of ϕ_v is a vortex surface consisting of vortex lines. Given a time series of the velocity–vorticity field obtained by solving (2.3) and (2.4), the calculation of the VSF can be implemented as a postprocessing step.

The two-time method (Yang & Pullin 2011) with source terms exerted on the immersed boundary (Tong *et al.* 2020) is used for calculating the temporal evolution of VSF. For each physical time step, it involves prediction and correction substeps. In the prediction substep, the temporary VSF solution is advanced in the physical time as

$$\frac{\partial \phi_v^*(\boldsymbol{x}, t)}{\partial t} + \boldsymbol{u}(\boldsymbol{x}, t) \cdot \boldsymbol{\nabla} \phi_v^*(\boldsymbol{x}, t) = q(\boldsymbol{x}), \quad t \geq 0, \tag{2.10}$$

where ϕ_v^* is a temporary VSF solution which can be deviated from the accurate VSF. In the correction substep, ϕ_v^* is transported along the frozen vorticity as

$$\frac{\partial \phi_v(\boldsymbol{x}, t; \tau)}{\partial \tau} + \boldsymbol{\omega}(\boldsymbol{x}, t) \cdot \boldsymbol{\nabla} \phi_v(\boldsymbol{x}, t; \tau) = q_\tau(\boldsymbol{x}), \quad 0 \leq \tau \leq T_\tau, \tag{2.11}$$

with

$$\phi_v(\boldsymbol{x}, t; \tau = 0) = \phi_v^*(\boldsymbol{x}, t). \tag{2.12}$$

In (2.10) and (2.11), the external VSF source terms $q(\boldsymbol{x})$ and $q_\tau(\boldsymbol{x})$ defined on Eulerian grid points are used to satisfy $\phi_v = \phi_v^B$ at the immersed boundary, with constant $\phi_v^B = 1$ on the plate. Finally, ϕ_v is updated by $\phi_v(\boldsymbol{x}, t; \tau = T_\tau)$ after the pseudo-time evolution, where T_τ is the maximum pseudo-time to ensure the convergence of ϕ_v in (2.11), and it is typically less than 100 times of Δt in (2.10).

As shown in figure 1(*b*), the VSF calculation is implemented in a subdomain $\Omega_\phi \in [-1.0, 7.5] \times [-1.5, 1, 5] \times [-3.5, 3.5]$ around the plate and near wake with strong vorticity. In Ω_ϕ, the high-resolution uniform mesh with $\Delta x = 0.02$ is set to ensure the smoothness of numerical VSF solutions. The velocity and vorticity fields in Ω_ϕ are interpolated from Ω through the quadratic Shepard method (Franke 1982).

To solve (2.10) and (2.11), the marching of t and τ is approximated by the second-order total-variation-diminishing Runge–Kutta method, and the convection term is calculated by the fifth-order weighted essentially non-oscillatory (WENO) scheme. The numerical diffusion in the WENO scheme serves as the numerical dissipation regularization for smoothing VSFs.

An initial VSF ϕ_{v0} needs to be specified to solve (2.10). The initial set-up implies that $\boldsymbol{\omega} = 0$ at $t = 0$, and $\boldsymbol{\omega}$ is generated at $t > 0$. Since the vorticity is dominated on the spanwise direction and $|\boldsymbol{\omega}|$ is close to an exact VSF at very early times (see Tong *et al.*

2020), we use $|\boldsymbol{\omega}|$ at $t = t_0 = 0.02$ to set

$$\phi_{v0}(\boldsymbol{x}, t_0; \tau = 0) = \sqrt{\frac{|\boldsymbol{\omega}(\boldsymbol{x})|}{|\boldsymbol{\omega}(\boldsymbol{x})|_{max}}}, \tag{2.13}$$

and then the initial VSF

$$\phi_{v0} = \phi_{v0}(\boldsymbol{x}, t_0; \tau = T_\tau) \tag{2.14}$$

at $t = t_0$ is obtained by solving (2.11), where $|\boldsymbol{\omega}(\boldsymbol{x})|_{max}$ denotes the maximum of $|\boldsymbol{\omega}(\boldsymbol{x})|$ in Ω_ϕ.

We remark that the numerical dissipation in the VSF convection can cause the artificial decay of the numerical VSF solution, so we compensate the numerical VSF before each physical time step in the two-time method based on the volume-averaged VSF $\langle\phi_{v0}\rangle$ and local $|\boldsymbol{\omega}|$. Since ϕ_v decays along with x, we empirically augment the VSF solution downstream as

$$\phi_v(\boldsymbol{x}, t) = \tilde{\phi}_v(\boldsymbol{x}, t)\gamma^{(\alpha_l|\boldsymbol{\omega}(\boldsymbol{x})|)/|\boldsymbol{\omega}(\boldsymbol{x})|_{max}}, \tag{2.15}$$

where $\tilde{\phi}_v$ denotes an intermediate VSF solution before the augmentation, $\gamma = \langle\phi_{v0}\rangle/\langle\tilde{\phi}_v(\boldsymbol{x}, t)\rangle > 1$ is an augmentation factor and $\alpha_l = l_x/(l_x + x^3)$ is an empirical parameter with the streamwise length l_x of Ω_ϕ. From numerical experiments, we find that this augmentation can effectively reduce the VSF dissipation or the volume shrinking of a particular VSF isosurface in the present simulation.

Starting from the constructed ϕ_{v0}, the numerical VSF solution is calculated by solving (2.10) and (2.11) with (2.15). The deviation of the numerical VSF from the exact VSF is monitored by the cosine of angle between the vorticity and VSF gradient as

$$\lambda_{\boldsymbol{\omega}} \equiv \frac{\boldsymbol{\omega} \cdot \nabla\phi_v}{|\boldsymbol{\omega}||\nabla\phi_v|}. \tag{2.16}$$

We find that the volumed-averaged VSF deviation $\langle|\lambda_{\boldsymbol{\omega}}|\rangle$ over Ω_ϕ is controlled to within approximately 4 %, indicating that the VSF solution is sufficiently accurate for the further characterization of vortex surfaces and modelling of forces.

3. Shedding of vortex surfaces

The discussion in this section is based on the typical Case 1, in which wake structures are dominated by a series of vortex pairs, and each pair contains two discrete vortex surfaces formed in a flapping period $T = 1/f$. We elucidate the shedding mechanism of vortex surfaces from the flapping plate using a particular VSF isosurface of $\phi_v = 0.3$. This isocontour-level selection considers the balance between the largest volume enclosed by VSF isosurfaces and the effective segmentation of discrete VSF isosurfaces in the wake.

From the morphology of vortex surfaces and lines, we divide the VSF evolution into three stages: (i) formation of the ring-like vortex surfaces during the first quarter of the flapping cycle; (ii) generation of spoon-like vortex surfaces during a half-cycle; (iii) periodic generation and shedding of spoon-like vortex surfaces.

3.1. *Formation of ring-like vortex surfaces*

At the initial time, the plate is located at $z_c = 0$ with the maximum angle of attack $\alpha = 30^\circ$. The plate heaves upwards to the highest point at $t = T/4$ by (2.2). In the meantime, the positive α decreases to 0° during this quarter cycle by (2.1). As shown in figure 2(*a*),

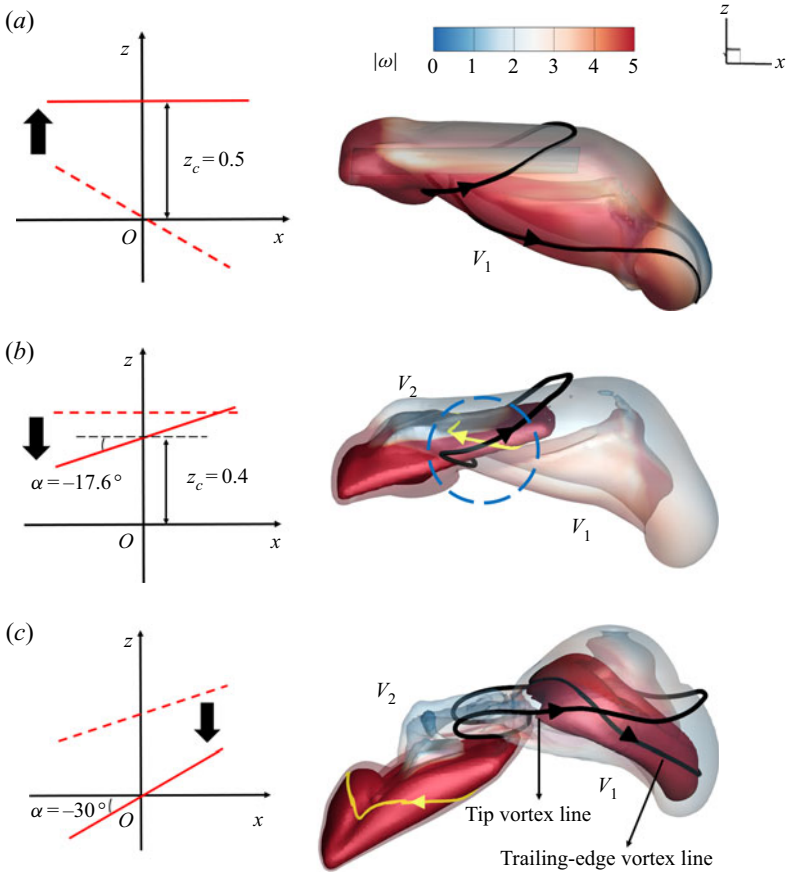

Figure 2. Temporal evolution of VSF isosurfaces during the downstroke. Left column: the red solid line denotes the plate at the present time and the red dashed line shows the previous location of the plate. Right column: the VSF isosurfaces are colour coded by the vorticity magnitude, with vortex lines integrated from points on the surface. Black and yellow lines represent the counterclockwise and clockwise vortex lines, respectively. (*a*) $t = 0.25T$, $\phi_v = 0.3$; (*b*) $t = 0.35T$, $\phi_v = 0.9$ (dark inner surface) and $\phi_v = 0.3$ (light outer surface). The black line is integrated on the surface of $\phi_v = 0.3$ and the yellow line is integrated on the surface of $\phi_v = 0.9$; (*c*) $t = 0.5T$, $\phi_v = 0.6$ (dark inner surface) and $\phi_v = 0.3$ (light outer surface). The tip vortex line is integrated on the surface of $\phi_v = 0.3$ and the other lines are integrated on the surface of $\phi_v = 0.6$.

the bulge-like vortex surface V_1 with counterclockwise vortex lines from the top view is generated around the tip and the trailing edge of the plate. The VSF isosurface is color-coded by $|\boldsymbol{\omega}|$, and in general ϕ_v is positively correlated to $|\boldsymbol{\omega}|$.

The plate begins to heave downwards at the end of the upstroke at $t = T/4$. During the downstroke, the vortex surface around the plate with negative α generates a secondary bulge V_2 consisting of clockwise vortex lines from the top view. As shown in figure 2(*b*), the inner vortical structure V_2 with $\phi_v = 0.9$ is wrapped by the outer structure V_1 with $\phi_v = 0.3$ at the trailing edge, where the additional isocontour level $\phi_v = 0.9$ is selected to represent a vortex surface in the high vorticity region. At the junction of V_1 and V_2 on the upper surface of the plate, the cancellation of clockwise and counterclockwise vortex lines significantly weakens the vorticity magnitude. Then, V_1 moves downstream and is gradually shed from the plate owing to the alternating sign of α. By contrast, in the flow

past a stationary plate with positive α, vortex surfaces with counterclockwise vortex lines are persistently rolled up from the tip region (see Tong *et al.* 2020).

During the downstroke in figure 2(*c*), we distinguish two types of vortex lines according to their original locations. The vortex lines generated at the trailing edge and the tip region are referred to as the trailing-edge and tip vortex lines, respectively. We observe that V_1 is dominated by the ring-like trailing-edge vortex lines in figure 2(*c*). The junction of outer V_1 with $\phi_v = 0.3$ and inner V_2 with an additional isocontour level $\phi_v = 0.6$ is dominated by the tip vortex lines with weak vorticity magnitude, and then V_1 is gradually shed off with disappearing tip vortex lines.

3.2. *Generation of spoon-like vortex surfaces*

In the downstroke period from $t = 0.25T$ to $0.75T$, the plate heaves from its highest to its lowest position, generating strong tip vortex lines on V_2. Subsequently, V_2 evolves into a spoon-like structure, composed of a bowl-like structure and a spinous handle in figure 3. Its geometry is very different from the ring-like V_1 generated in the first upstroke period from $t = 0$ to $0.25T$.

When the plate retains a negative α in the downstroke, vortex surface V_2 continuously deforms in the leading-edge and tip regions. We divide V_2 into two parts by the isosurface of $\omega_x = 0$ (Tong *et al.* 2020), where ω_x is the streamwise vorticity component. In figure 3(*a*), the upstream part generated from the leading edge is referred to as the leading-edge vortex (LEV), and the downstream part generated from the tip region is referred to as the tip vortex (TIV). The TIV lines connecting the LEV and TIV constitute the main structure in the later evolution. The trailing-edge vortex lines are wrapped up by outer TIV lines. They gradually vanish owing to the vorticity cancellation under the intensive swirling motion induced by TIV lines with strong entrainment (Taira & Colonius 2009; Lee *et al.* 2012).

At the end of downstroke, the plate heaves upwards, generating another counterclockwise vortex bulge V_3 in figure 3(*b*,*c*). In the meantime, V_2 is shed off from the plate, which is similar to the shedding of V_1 in § 3.1 owing to the cancellation of opposite vorticities in the region between V_2 and V_3. In the evolution of V_2 in figure 3(*a*), the ring-like TIV lines are lifted in the upstream (marked by the light grey arrow) owing to the continuous rolling up of vortex surfaces at the leading edge during the downstroke period. The TIV lines are stretched in the streamwise direction by the mean shear, and are compressed in the spanwise direction by the induced velocity of two TIVs downstream (marked by dark grey arrows). The TIVs then evolve into spoon-like structures in figure 3(*b*) with the merging of two TIVs, which was not observed for the VSF evolution of the flow past a stationary plate in Tong *et al.* (2020). Subsequently, V_2 is shed off as a discrete spoon-like vortex surface in the wake in figure 3(*c*).

3.3. *Periodic shedding of vortex surfaces*

The shedding of spoon-like vortex surfaces from the flapping plate is periodic. In a time period of $0.5T$, the counterclockwise or clockwise vortex surface is created during the upstroke or downstroke, respectively. Then, the newly generated, discrete vortex surfaces propagate downstream.

Figure 4 depicts the top and side views of the VSF isosurface of $\phi_v = 0.3$ at $t = 3T$. There are two sets of discrete vortex surfaces propagating towards the positive and negative z-directions. Each set is composed of discrete vortex surfaces generated at the end of upstroke or downstroke of the plate. From the top view in figure 4(*a*), a row of circular

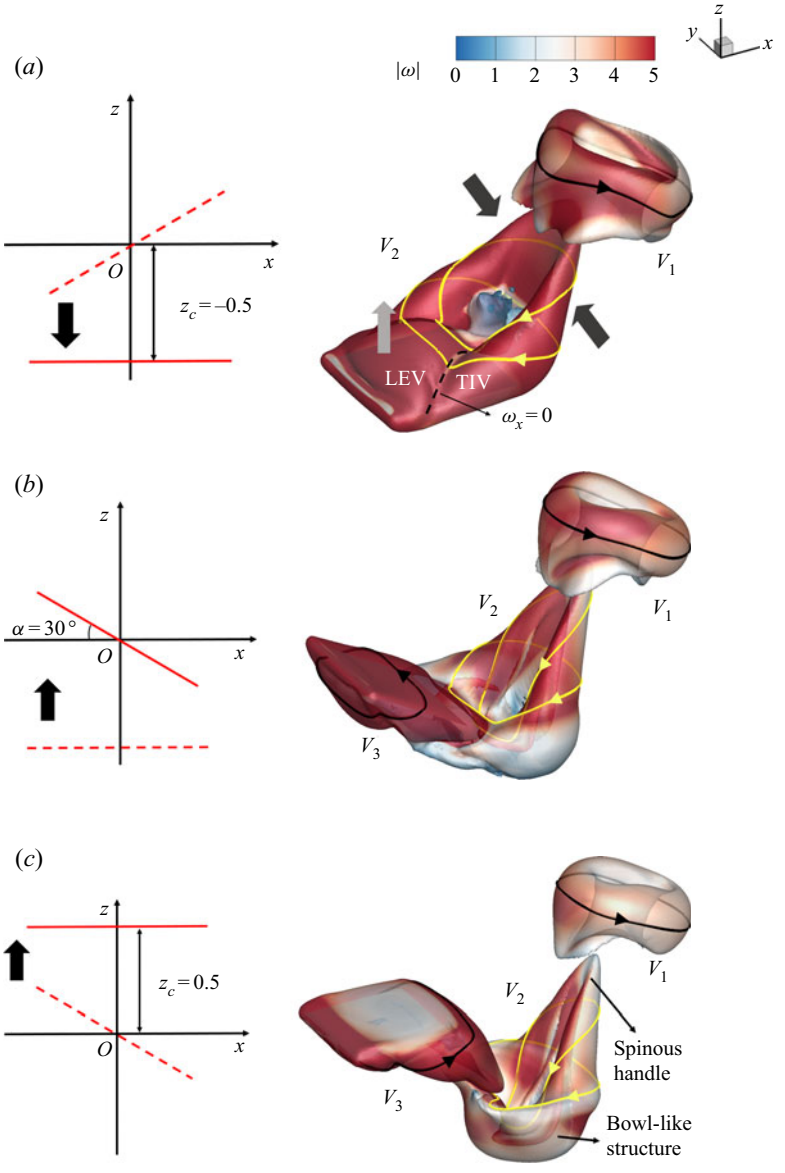

Figure 3. Temporal evolution of the VSF isosurface of $\phi_v = 0.3$ during formation and shedding of spoon-like structures. The notations are the same as in figure 2: (*a*) $t = 0.75T$; (*b*) $t = T$; (*c*) $t = 1.25T$.

wake structures are compressed in the spanwise direction induced by TIVs. From the side view in figure 4(*b*), almost all the spoon-like vortex surfaces consist of TIV lines, except ring-like V_1 dominated by trailing-edge vortex lines.

We extract and label the discrete vortex surfaces by an automatic searching and flooding algorithm, and then track their evolution in the wake. At a particular time t, we count the total number, $N(t)$, of discrete vortex surfaces, e.g. $N(t = 3T) = 7$ in figure 4(*b*). For the $N(t)$ vortex surfaces, the ith one is labelled as V_i in an ascending sequence according to its shedding time, i.e. $i = 1$ is for the first shedding surface, and $i = N(t)$ is for the surface enclosing the plate.

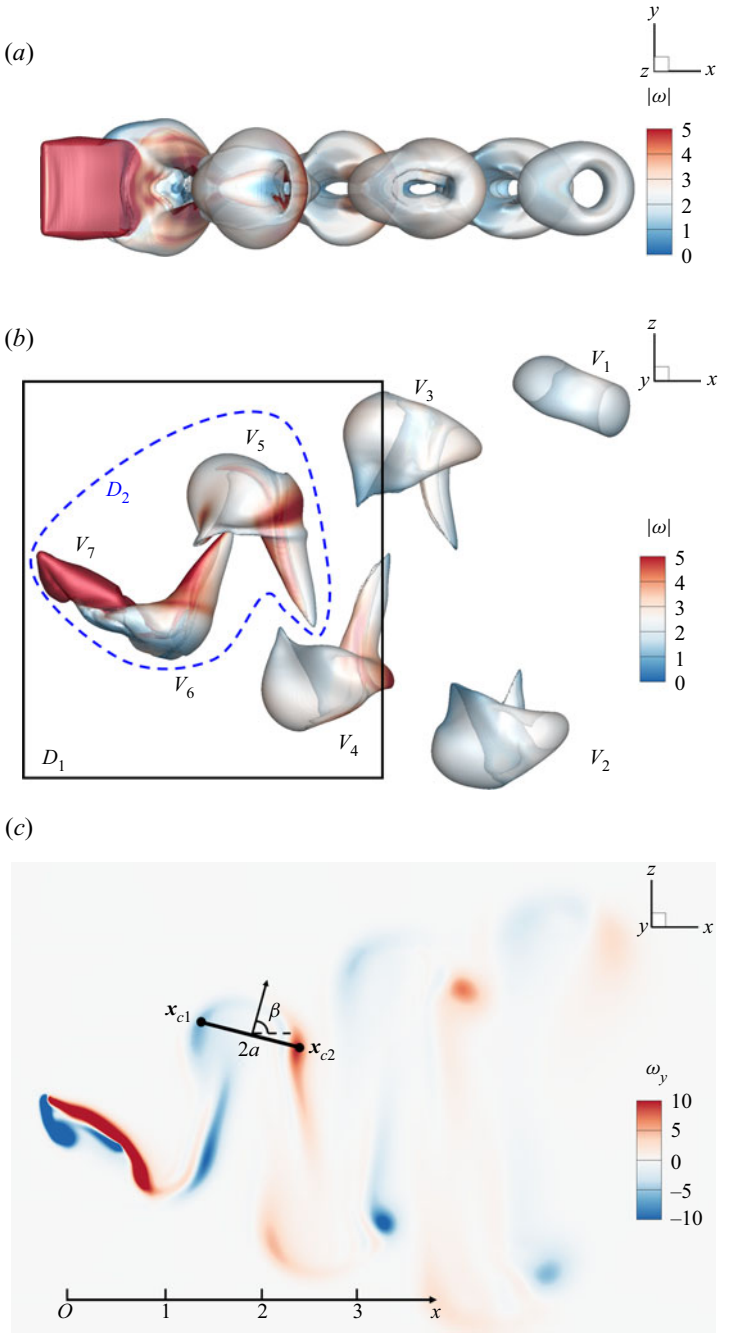

Figure 4. The VSF isosurface of $\phi_v = 0.3$ at $t = 3T$ in (*a*) top view and (*b*) side view, where D_1 (black solid line) and D_2 (blue dashed line) are two types of integral domains enclosing the plate for calculating the total force in (4.3). (*c*) Contour of the spanwise vorticity on the spanwise symmetry plane at $y = 0$.

The evolution of spoon-like vortex surfaces in the wake in figure 4(*b*) can be roughly split into two phases. First, the vortex surface evolves with the local induction of adjacent vortex surfaces. The upstream part of a vortex surface (e.g. V_4) is lifted to form a 'nose' by the induction of TIVs of its upstream spoon-like vortex surface (e.g. V_5), similar to the vortex contrail structure observed in Dong *et al.* (2006). In the second phase, the vortex surface evolves almost independently owing to the diminishing induction effect among separating vortex surfaces. As the spoon-like vortex surface convects downstream, its upstream nose-like structure and downstream handle-like structure are gradually smoothed out, evolving into a ring-like vortex surface (e.g. V_2).

The discrete vortex surface in the wake was simplified as a vortex ring for further theoretical analysis, which is detailed in Appendix B. As sketched in figure 4(*c*), the radius a and the inclination angle β of the vortex ring are determined by the spanwise vorticity ω_y on the spanwise symmetry plane.

4. Estimating forces from the wake

4.1. *Impulse theory for a finite domain*

From the wake information of a flapping plate, we estimate aerodynamic forces acting on the plate using the impulse theory (see Wu 1981; Wu *et al.* 2015). In a three-dimensional incompressible viscous flow, the total force on a moving body is

$$\boldsymbol{F} = -\frac{\mathrm{d}\boldsymbol{I}_{f\infty}}{\mathrm{d}t} + \frac{1}{2}\frac{\mathrm{d}}{\mathrm{d}t}\int_{\partial B} \boldsymbol{x} \times (\boldsymbol{n} \times \rho \boldsymbol{u})\,\mathrm{d}S, \tag{4.1}$$

where

$$\boldsymbol{I}_{f\infty} = \tfrac{1}{2}\int_{\mathcal{V}_{f\infty}} \boldsymbol{x} \times \rho\boldsymbol{\omega}\,\mathrm{d}V \tag{4.2}$$

is the vortical impulse in the entire fluid domain $\mathcal{V}_{f\infty}$, ∂B is the body surface and $\boldsymbol{n}$ is the unit surface normal.

From the impulse theory for a finite domain $\mathcal{V}_f$ bounded by surface Σ in flows with discrete wake vortices (see Wu *et al.* 2007; Kang *et al.* 2018), the total force on the plate becomes

$$\boldsymbol{F} = -\frac{\mathrm{d}\boldsymbol{I}_f}{\mathrm{d}t} - \boldsymbol{L} + \boldsymbol{F}_{\partial B} + \boldsymbol{F}_{\omega_n} + \boldsymbol{F}_{\Sigma}. \tag{4.3}$$

Here,

$$\boldsymbol{I}_f = \tfrac{1}{2}\int_{\mathcal{V}_f} \boldsymbol{x} \times \rho\boldsymbol{\omega}\,\mathrm{d}V, \tag{4.4}$$

denotes the vortical impulse in the finite domain $\mathcal{V}_f$,

$$\boldsymbol{L} = \int_{\mathcal{V}_f} \rho\boldsymbol{\omega} \times \boldsymbol{u}\,\mathrm{d}V, \tag{4.5}$$

denotes the integral of the Lamb vector $\boldsymbol{\omega} \times \boldsymbol{u}$,

$$\boldsymbol{F}_{\partial B} = \tfrac{1}{2}\int_{\partial B} \boldsymbol{x} \times (\boldsymbol{n} \times \rho\boldsymbol{a})\,\mathrm{d}S + \tfrac{1}{2}\int_{\partial B} \boldsymbol{x} \times \rho\boldsymbol{u}\omega_n\,\mathrm{d}S, \tag{4.6}$$

denotes the force contributed by the body motion and deformation with the acceleration $\boldsymbol{a}$ of the body and the vorticity component ω_n normal to ∂B,

$$\boldsymbol{F}_{\omega_n} = \tfrac{1}{2}\int_{\Sigma} \boldsymbol{x} \times \rho\boldsymbol{u}\omega_n\,\mathrm{d}S, \tag{4.7}$$

denotes the force due to the normal vorticity on Σ with the vorticity component ω_n normal to Σ and

$$\boldsymbol{F}_{\Sigma} = \frac{1}{2}\int_{\Sigma} (\boldsymbol{x} \times \rho\boldsymbol{\sigma} + \boldsymbol{\tau})\,\mathrm{d}S \tag{4.8}$$

is the viscous force calculated on Σ with the diffusive vorticity flux $\boldsymbol{\sigma} = \nu\partial\boldsymbol{\omega}/\partial n$ and the shear stress $\boldsymbol{\tau} = \mu\boldsymbol{\omega} \times \boldsymbol{n}$. We validate that the relative discrepancy between the total forces calculated from (4.3) in the impulse theory and directly from the DNS data for the present cases is only approximately 1 %.

Some terms in (4.3) can be neglected in the present cases. The thin plate with negligible deformation implies $\boldsymbol{F}_{\partial B} = 0$ owing to the vanishing ω_n on the body surface and opposite $\boldsymbol{n}$ on the top and bottom plates. For high Re, $\boldsymbol{F}_{\Sigma}$ for the viscous effect is neglected. In the present simulation with $Re = 200$, the contribution of $\boldsymbol{F}_{\Sigma}$ on the total force is only approximately 0.1 %. Thus, the total force of the flapping plate is determined by the vortical impulse, the Lamb-vector integral and the surface integral $\boldsymbol{F}_{\omega_n}$ over the boundary of a finite fluid domain in (4.3).

4.2. *Impulse theory based on vortex surfaces*

In order to further simplify (4.3), it is crucial to choose an appropriate domain boundary Σ to minimize $\boldsymbol{F}_{\omega}$ in (4.7).

First, Kang *et al.* (2018) proposed a strict constraint, $\boldsymbol{\omega} = 0$ at and near Σ, to eliminate $\boldsymbol{F}_{\omega_n}$ in the minimum-domain impulse theory, but this condition is hard to satisfy in three-dimensional flows. Second, a simple domain facilitates the calculation of the surface integral in $\boldsymbol{F}_{\omega_n}$, e.g. a rectangular domain $\mathcal{V}_f$ enclosing the body (Wang *et al.* 2013). However, $\boldsymbol{F}_{\omega_n}$ is non-vanishing in (4.3), e.g. the positive contribution of $\boldsymbol{F}_{\omega_n}$ to the time-averaged thrust can be approximately 50 % in our Case 1 with $\mathcal{V}_f = D_1$ enclosed by the black solid line in figure 4(*b*). Third, an integral domain cutting a small portion of vorticity is another option to minimize $\boldsymbol{F}_{\omega}$. Li & Lu (2012) chose a domain enclosing two discrete vortical structures near the plate, e.g. $\mathcal{V}_f = D_2$ enclosed by the blue dashed curve in figure 4(*b*), but D_2 should move with the vortical structure at different times and its geometry varies with different flow parameters, so it has to be determined *ad hoc* for different cases.

Compared with the existing options for Σ, the VSF isosurface is a more natural choice, because it has $\boldsymbol{F}_{\omega_n} = 0$ with $\omega_n = 0$ on Σ and evolves with time. Based on the VSF, we choose Σ as a particular vortex surface Σ_b enclosing the plate in figure 5. In this way, (4.3) is simplified to

$$\boldsymbol{F} = -\frac{\mathrm{d}\boldsymbol{I}_b}{\mathrm{d}t} - \boldsymbol{L}_b, \tag{4.9}$$

where

$$\boldsymbol{I}_b = \frac{1}{2}\int_{\mathcal{V}_b} \boldsymbol{x} \times \rho\boldsymbol{\omega}\,\mathrm{d}V \tag{4.10}$$

denotes the vortical impulse in a finite fluid domain $\mathcal{V}_b$ enclosed by Σ_b, and

$$\boldsymbol{L}_b = \int_{\mathcal{V}_b} \rho\boldsymbol{\omega} \times \boldsymbol{u}\,\mathrm{d}V \tag{4.11}$$

denotes the Lamb-vector integral over $\mathcal{V}_b$. As sketched in figure 5, $\boldsymbol{F}$ is only determined by the velocity–vorticity field within $\mathcal{V}_b$. Then we obtain the thrust force

$$F_T = \frac{\mathrm{d}I_{b,x}}{\mathrm{d}t} + L_{b,x}, \tag{4.12}$$

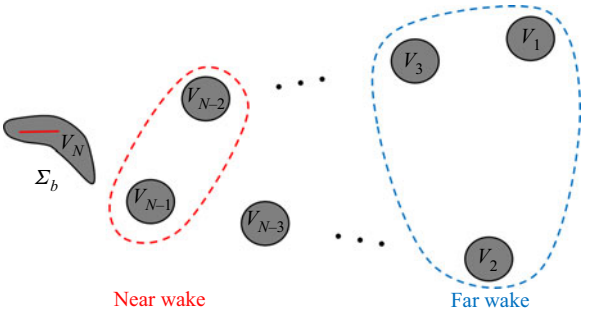

Figure 5. Sketch of vortex surfaces in the near wake and far wake of a flapping plate.

where $I_{b,x}$ and $L_{b,x}$ are the streamwise components of $\boldsymbol{I}_b$ and $\boldsymbol{L}_b$, respectively.

In the present cases, the time-averaged thrust can be determined by

$$\bar{F}_T = \overline{\frac{\mathrm{d}I_{b,x}}{\mathrm{d}t}} + \bar{L}_{b,x} \tag{4.13}$$

over a half-period $T_f = T/2$ within either one downstroke or upstroke owing to the periodic flapping motion of the plate, where $\bar{f}$ denotes the time average of a function f over T_f. Without loss of generality, we choose one downstroke period to estimate $\bar{F}_T$. Figure 6 sketches the formation and shedding of the ith vortex surface V_i from the plate with $i \geq 3$. We define the beginning time $t_i' = T/4 + (i-2)T_f$ of downstroke in figure 6(a), the end time $t_i'' = T/4 + (i-1)T_f$ of downstroke in figure 6(b) and the shedding time $t_i^s \approx t_i'' + T_f = T/4 + iT_f$ of V_i in figure 6(c) when V_i is just shed from the plate.

During the downstroke from $t = t_i'$ to $t = t_i''$ for the generation of V_i, the Lagrangian-like evolution of Σ_b is marked by the red dashed curves in figure 6(a,b). Since the shedding of spoon-like vortex surfaces from the flapping plate is periodic, we estimate

$$\overline{\frac{\mathrm{d}I_{b,x}}{\mathrm{d}t}} = \frac{I_{b,x}(t_i'') - I_{b,x}(t_i')}{T_f} \approx \frac{I_{i-1,x}(t_i'')}{T_f} \approx \frac{I_{i,x}^s}{T_f} \tag{4.14}$$

in (4.13), where $I_{i,x}^s$ denotes the streamwise component of the vortical impulse

$$\boldsymbol{I}_i^s = \tfrac{1}{2}\int_{V_i} \boldsymbol{x} \times \rho\boldsymbol{\omega}\,\mathrm{d}V \tag{4.15}$$

for V_i at its shedding time $t = t_i^s$, and all the $I_{i,x}^s = I_x^s$ are the same for $3 \leq i \leq N$. Then, the time-averaged thrust

$$\bar{F}_T = \frac{I_x^s}{T_f} + \bar{L}_{b,x} \tag{4.16}$$

acting on the plate can be estimated based on the velocity–vorticity field within $\mathcal{V}_b$ enclosed by the vortex surface.

For the further application, we can also estimate the force only from the shedding vortex surfaces in the near wake and far wake in §§ 4.3 and 4.4, respectively. As sketched in figure 5, the near-wake region has the discrete vortex surfaces close to the plate, and the far-wake region is remote from the plate.

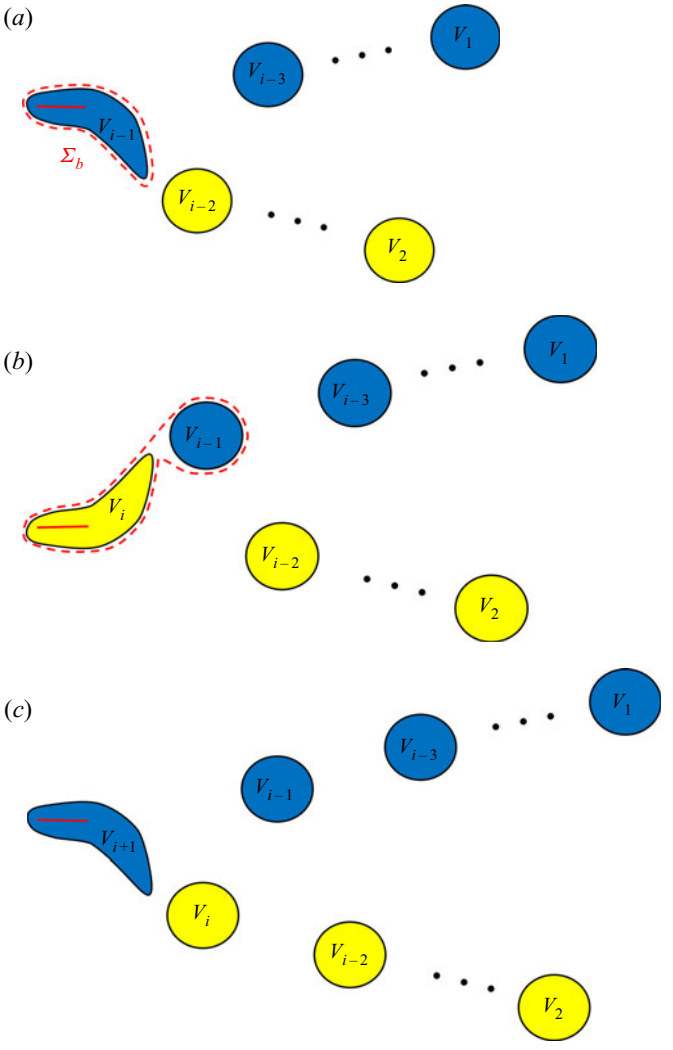

Figure 6. Sketch of formation and shedding of vortex surface V_i at different times: (*a*) $t = t_i'$, the beginning time of downstroke; (*b*) $t = t_i''$, the end time of downstroke; (*c*) $t = t_i^s$, the shedding time of V_i. The vortex surfaces with counterclockwise and clockwise vortex lines are coloured in blue and yellow, respectively. The Lagrangian-like evolution of Σ_b labelled at $t = t_i'$ is marked by the red dashed curves.

4.3. *Estimating thrust from the near wake*

In order to estimate time-averaged forces on the plate from the wake, we extend $\bar{L}_{b,x}$ in (4.16) based on the vortex surface enclosing the plate to an expression based on discrete vortex surfaces in the wake. Since the Lamb-vector integral

$$\int_{\mathcal{V}_{f\infty}} \rho\boldsymbol{\omega} \times \boldsymbol{u}\,\mathrm{d}V = \boldsymbol{L}_b + \boldsymbol{L}_{wake} = 0 \tag{4.17}$$

vanishes in $\mathcal{V}_{f\infty}$ (Wu *et al.* 2015), which is also validated by our DNS, we obtain

$$\boldsymbol{L}_b = -\boldsymbol{L}_{wake}. \tag{4.18}$$

Considering the downstroke for generating V_i from $t = t_i'$ to $t = t_i''$ in figures 6(*a*) and 6(*b*), we approximate

$$\boldsymbol{L}_{wake} = \sum_{j=1}^{i-2} \boldsymbol{L}_j \tag{4.19}$$

as the sum of the Lamb-vector integral

$$\boldsymbol{L}_j = \int_{V_j} \rho \boldsymbol{\omega} \times \boldsymbol{u} \, \mathrm{d}V, \tag{4.20}$$

for the jth discrete vortex surface V_j in the wake.

Since the spoon-like vortex surface with finite $\boldsymbol{L}_j$ evolves towards a ring-like one with $\boldsymbol{L}_j \approx 0$ in the far wake, $\boldsymbol{L}_j$ decays quickly in the downstream. Hence, we estimate

$$\boldsymbol{L}_{wake} \approx \boldsymbol{L}_{i-2} \tag{4.21}$$

from the near-wake vortex surface in the downstroke, as shown in figures 6(*a*) and 6(*b*), and then have

$$\bar{L}_{b,x} = -\bar{L}_{wake,x} \approx -\bar{L}_{i-2,x}, \tag{4.22}$$

where $\bar{L}_{wake,x}$ and $\bar{L}_{i-2,x}$ denote the time-averaged streamwise components of $\boldsymbol{L}_{wake}$ and $\boldsymbol{L}_{i-2}$, respectively.

Identified by the VSF isosurface at a given time, there are $N(t)$ vortex surfaces in an instantaneous flow field, and surface V_{N-1} is shed into the wake in figure 5. Substituting (4.22) into (4.16) and taking $i = N - 1$ yields

$$\bar{F}_T = \frac{I_x^s}{T_f} - \bar{L}_{N-3,x}. \tag{4.23}$$

Then, we approximate

$$\bar{L}_{N-3,x} = \frac{1}{T_f} \int_{t_{N-1}'}^{t_{N-1}''} L_{N-3,x} \, \mathrm{d}t \approx \frac{L_{N-3,x}(t_{N-1}') + L_{N-3,x}(t_{N-1}'')}{2}, \tag{4.24}$$

where $L_{N-3,x}(t_{N-1}')$ and $L_{N-3,x}(t_{N-1}'')$ denote the streamwise components of the Lamb-vector integral for V_{N-3} at $t = t_{N-1}'$ and $t = t_{N-1}''$, respectively. Considering the periodic shedding of vortex surfaces from the flapping plate in T_f (also see figure 6), we have $L_{N-3,x}(t_{N-1}') \approx L_{N-1,x}(t_{N-1}^s)$ and $L_{N-3,x}(t_{N-1}'') \approx L_{N-2,x}(t_{N-1}^s)$. Finally, (4.23) is re-expressed by

$$\bar{F}_T = \frac{I_x^s}{T_f} - \frac{L_{N-1,x} + L_{N-2,x}}{2}, \tag{4.25}$$

where all the terms on the right-hand side are determined at $t = t_{N-1}^s$.

The thrust model (4.25) from the near wake is validated by the DNS result calculated from (2.7). From (4.25), the mean thrust coefficient $\bar{C}_T$ is estimated as

$$\bar{C}_T^N = \bar{C}_T^I + \bar{C}_T^L. \tag{4.26}$$

Here, the force contribution from the vortical impulse is

$$\bar{C}_T^I = \frac{I_x^s}{\frac{1}{2}\rho U^2 R_A T_f c^2}, \tag{4.27}$$

Case	DNS	Near-wake model	Impulse model	Far-wake model	Vortex-ring model
1	0.765	0.738	0.850	0.724	1.056
2	0.601	0.632	0.748	0.673	1.008
3	0.347	0.370	0.448	0.384	0.588
4	0.866	0.811	0.921	0.790	1.468

Table 2. Comparison of $\bar{C}_T$ from DNS, $\bar{C}_T^N$ from the near-wake model, $\bar{C}_T^I$ from the impulse model, $\bar{C}_T^F$ from the far-wake model and $\bar{C}_T^R$ from the vortex-ring model for estimating the thrust coefficient in the cases with different parameters in table 1.

and the contribution from the Lamb vector is

$$\bar{C}_T^L = -\frac{L_{N-1,x} + L_{N-2,x}}{\rho U^2 R_A c^2}. \tag{4.28}$$

Table 2 compares the mean thrust coefficients calculated from (2.8), (4.26) and (4.27) in Cases 1–4 listed in table 1 with the varying angle of attack, flapping frequency and Reynolds number. It is noted that the wake in the four cases consists of discrete vortex surfaces, and the force estimation for the wakes with complex topology, Cases 5 and 6, is discussed in Appendix C. We find that $\bar{C}_T^N$ estimated from the near-wake model agrees well with the DNS result $\bar{C}_T$ and the relative errors

$$\varepsilon = \frac{|\bar{C}_T^{model} - \bar{C}_T|}{\bar{C}_T} \tag{4.29}$$

are approximately 5 %, where $\bar{C}_T^{model}$ denotes a model estimation of $\bar{C}_T$. Additionally, we validate that the near-wake model works well with $\varepsilon \approx 8\,\%$ for the case of a heaving and pitching plate around the leading edge with $Re = 200$, $St = 0.6$ and discrete wake topology in Li & Lu (2012).

By contrast, $\bar{C}_T^I$ only considering the vortical-impulse contribution is obviously overestimated. Hence, the negative $\bar{C}_T^L$ contributed from the Lamb vector provides a necessary correction to the impulse model, improving the prediction accuracy of $\bar{C}_T$ by approximately 12 %.

In general, the VSF $\phi_v \in [0, 1]$ is positively correlated with the vorticity magnitude. We choose the particular $\phi_v = 0.3$ to discretize the vortex wake. The region enclosed by the isosurface of $\phi_v = 0.3$ captures approximately 90 % of the vortical impulse of shedding vortex surfaces in the entire domain. Thus, we find that the calculation of I_x^s in (4.26) for a single vortex surface is slightly underestimated by 2 %, assuming the similar I_x^s distribution of all the five vortex surfaces in the wake in figure 4.

For comparison, we also estimate $\bar{C}_T$ from the near-wake model (4.26) based on the isosurface of Eulerian vortex criteria $|\boldsymbol{\omega}|$ and λ_2, and obtain relatively large $\varepsilon = 17\,\%$ and $\varepsilon = 32\,\%$, respectively. The major reason is that the isosurface of $|\boldsymbol{\omega}|$ or λ_2 can have a notable difference from the vortex surface (Yang & Pullin 2011), so the contribution from the surface integral (4.7) cannot simply be neglected for these isosurfaces. We remark that the choice of the isocontour level of $|\boldsymbol{\omega}|$ or λ_2 is *ad hoc* for vortex identification, and we have tuned $|\boldsymbol{\omega}|$ and λ_2 to minimize their corresponding ε.

In addition, the vortex-ring model (see Lauder & Drucker 2002; Nauen & Lauder 2002; Li & Lu 2012) can estimate the mean thrust using the vortical impulse $I_v = \rho\pi\Gamma a^2$ of a vortex ring, where Γ is the circulation of the vortex ring. In Appendix B, we simplify

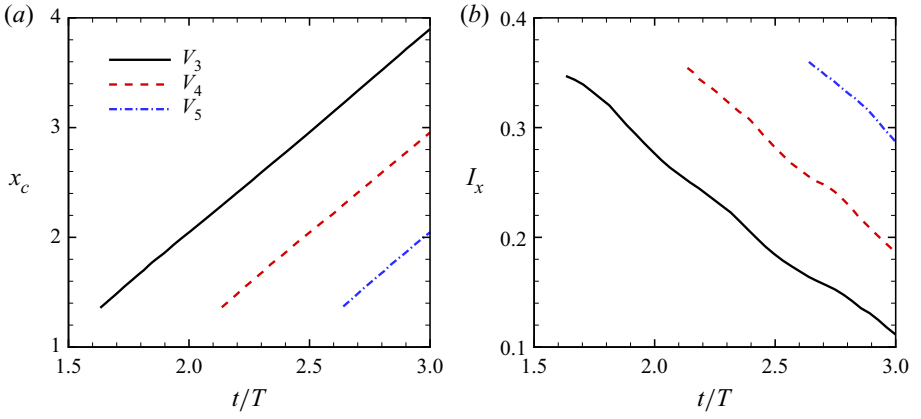

Figure 7. Temporal evolution of (*a*) streamwise vortex centre x_c and (*b*) streamwise impulse I_x of discrete vortex surfaces in the wake.

the spoon-like vortex surface in figure 4 to the vortex ring, and determine the mean thrust coefficient $\bar{C}_T^R$ from the modelled vortex ring. In table 2, $\bar{C}_T^R$ is overestimated and has larger discrepancies than other models for our cases, perhaps owing to the over-simplification of the spoon-like vortex surfaces in figures 3 and 4 as vortex rings. We find that the time-averaged streamwise vortical impulse of ring-like V_1 dominated by circular trailing-edge vortex lines is approximately 40 %–50 % larger than that of the spoon-like vortex surfaces with kinked tip vortex lines.

4.4. *Estimating thrust from the far wake*

From the practical viewpoint, estimating forces on the moving body from the far wake is very useful in the experimental investigation of biological locomotion (Lauder & Drucker 2002; Spedding *et al.* 2003) and underwater vehicles (Jiménez *et al.* 2010). As indicated in figure 4, a pair of discrete vortex surfaces are shed form the plate within T, and the wake is dominated by two rows of discrete vortex surfaces. The evolution of vortex pairs in the wake is similar owing to their periodic formation and shedding process. Thus, it is possible to estimate forces based on two arbitrary vortex surfaces in the far wake.

We define the geometrical centre of vortex surface V_i as

$$\boldsymbol{x}_{c,i} = \frac{\displaystyle\int_{V_i} \boldsymbol{x}\,\mathrm{d}V}{\displaystyle\int_{V_i} \mathrm{d}V}. \tag{4.30}$$

Figure 7(*a*) shows that the vortex centre moves downstream with a uniform velocity, and the streamwise vortical impulse also linearly decays for all the discrete vortex surfaces. These linear relations are utilized to infer I_x^s from the far wake.

We approximate the shedding location $x_{c,s} = 1.5$ for all the discrete vortex surfaces, corresponding to the position where I_x^s is obtained. Given two arbitrary vortex surfaces V_a and V_b with $a, b = 3, \ldots, N-1$ in the wake, we estimate the initial streamwise vortical impulse I_x^s as

$$I_x^s \approx I_x^F = I_{a,x} + \frac{I_{a,x} - I_{b,x}}{x_{c,b} - x_{c,a}}(x_{c,a} - x_{c,s}), \tag{4.31}$$

where $x_{c,a}$ and $x_{c,b}$ respectively denote streamwise vortex centres of V_a and V_b, and $I_{a,x}$ and $I_{b,x}$ respectively denote streamwise vortical impulses of V_a and V_b. Then, we estimate the mean thrust coefficient

$$\bar{C}_T^F = \frac{A_L I_x^F}{\frac{1}{2}\rho U^2 R_A T_f c^2} \tag{4.32}$$

from the far wake with small a and b, where $A_L = 0.85$ is an attenuation factor for the Lamb-vector correction. In this far-wake model, we estimate the thrust contributed from the vortical impulse without explicitly considering the Lamb-vector integral, because it is difficult to predict $\boldsymbol{L}$ at the shedding time from the far wake owing to the fast decay of $\boldsymbol{L}$ downstream. In order to incorporate the negative contribution of $\boldsymbol{L}$ to $\bar{C}_T$, we alternatively apply the factor $A_L = 0.85$ in (4.32), which is estimated based on the overall ratio of $\bar{C}_T^N$ from the near-wake model and $\bar{C}_T^I$ from the impulse model listed in table 2.

The far-wake model predictions from (4.32) with $a = 4$ and $b = 3$ generally agree with the DNS results in table 2, and the relative errors $\varepsilon \approx 9\,\%$ are, reasonably, larger than those in the near-wake model. The thrust predictions with different a and b are very similar within $\pm 3\,\%$ variation. Furthermore, we can also calculate I_x^F and then estimate $\bar{C}_T^F$ from the Lagrangian history of a single vortex surface at different locations at two times within a small time interval.

The far-wake model (4.32) implies that the thrust of the flapping plate is determined by the vortical impulse generated during the flapping motion, and the shedding vortex surface with larger I_x^F can generate larger thrust on the moving body (Spedding *et al.* 2003; Li & Lu 2012), which can guide the optimization of the kinematics parameters of the flapping plate in (2.1) and (2.2) to increase the thrust of the flapping plate by shedding the vortex surface with larger I_x^F.

Thus, we provide a possible approach to estimate thrust using only two vortex surfaces in the wake, which can facilitate the estimation of the state of the moving body in experimental investigation and practical applications. In the experimental implementation, the particle image velocimetry (PIV) can be used to measure the three-dimensional flow field in the wake (Buchholz & Smits 2008; Mendelson & Techet 2015). The PIV data are usually subject to noise, so the time series of raw PIV data need to be corrected, e.g. using the divergence-free smoothing method (Wang *et al.* 2016). Subsequently, the boundary-constraint method (Xiong & Yang 2017) can be applied to construct VSFs, then the thrust is estimated based on vortex surfaces in the wake. On the other hand, significant challenges still exist in the implementation, e.g. the incompleteness of velocity/vorticity measurement, accuracy of VSF calculation from under-revolved experimental data and the uncertainty quantification of the force estimation.

5. Conclusions

We investigate the VSF evolution in flows past a flapping plate with a low aspect ratio and estimate the time-averaged thrust from shedding vortex surfaces in the wake. The immersed boundary method is used to obtain the velocity–vorticity field, and the two-time method with source terms is applied to calculate the VSF solution.

The VSF evolution can be roughly split into three stages based on the morphology of vortex surfaces and lines. During the first quarter of the flapping cycle, a vortex bulge dominated by counterclockwise vortex lines is formed, and then it is shed from the trailing edge due to the vorticity cancellation between two adjacent vortex surfaces and evolves into a circular vortex ring in the wake. During the following half-flapping cycle, a spoon-like vortex surface dominated by TIV lines is generated. In the late stage,

the spoon-like vortex surfaces are periodically created and shed during the alternating upstroke and downstroke. Two sets of vortex surfaces propagate downstream in the wake, and the spoon-like vortex surface gradually evolves into ring-like vortex in the far wake.

We develop near-wake and far-wake models to estimate the time-averaged thrust from the shedding vortex surfaces in the wake. First, we choose a particular vortex surface as the integral domain in the finite-domain impulse theory, so that the force on the moving body is determined by the vortical impulse and Lamb-vector integral of the vortex surface enclosing the body. Then, the force estimation is extended to that from the discrete vortex surfaces in the wake. Here, the vortical impulse is obtained at the vortex shedding time, and the force contribution from the Lamb-vector integral enclosing the body is approximated by the two discrete vortex surfaces close to the plate. Thus, the time-averaged thrust coefficient can be estimated from the near wake, and our model estimation agrees well with the DNS result in various cases with different angles of attack, flapping frequencies and Reynolds numbers. The relative errors are approximately 5 %, and they are smaller than those from predictions of the impulse model and the vortex-ring model, which implies the importance of incorporating effects of the Lamb vector in the thrust model and the over-simplification of the spoon-like vortex surfaces as vortex rings.

Furthermore, we estimate the time-averaged thrust from two arbitrary vortex surfaces in the far wake based on the self-similar formation and evolution process of vortex surfaces in the periodic flapping motion. The relative errors of the far-wake model are approximately 9 %, which are larger than the near-wake errors owing to the uncertainty of the force correction from the Lamb-vector integral. This model provides a possible approach to inferring the state of the moving body in experimental investigation and practical applications.

We remark that the thrust models developed in this study are restricted to a flapping plate with discrete vortex surfaces in the wake. In future work, the VSF method should be extended to characterize the evolution of vortex surfaces and estimate forces from more complex vortex wakes for higher R_A and St, in which the vortical structures are interconnected. With further improvement, the proposed thrust model is expected to be applied to temporally resolved PIV data in experimental and practical applications.

Acknowledgements. Numerical simulations were carried out on the TH-2A supercomputer in Guangzhou, China.

Funding. This work has been supported in part by the National Natural Science Foundation of China (Nos. 91952108, 11925201, 11988102 and 91841302) and the Xplore Prize.

Declaration of interests. The authors report no conflict of interest.

Author ORCIDs.
Yue Yang https://orcid.org/0000-0001-9969-7431;
Shizhao Wang https://orcid.org/0000-0002-5111-5356.

Appendix A. Mesh convergence test

The numerical implementation of the immersed boundary method in the present study has been validated in previous studies, including the three-dimensional flow past a three-dimensional stationary plate (Wang & Zhang 2011) and flapping plate (Wang *et al.* 2013, 2019). Additional validations for the effectiveness of the present mesh spacing and computational domain are given below.

We simulated the flow past a flapping plate on four meshes M_1, M_2, M_3 and M_4 with the minimum spacings $\Delta x = 0.02$, 0.015, 0.0125 and 0.01, respectively. The detail of

Mesh	Computational domain	Minimum Δx
M_1	$[-11.84, 19.84] \times [-16, 16] \times [-16, 16]$	0.02
M_2	$[-13.2, 21.6] \times [-18, 18] \times [-18, 18]$	0.015
M_3	$[-14, 22] \times [-18, 18] \times [-18, 18]$	0.0125
M_4	$[-15.04, 22.08] \times [-18.88, 18.88] \times [-18.88, 18.88]$	0.01

Table 3. Mesh parameters in the convergence test.

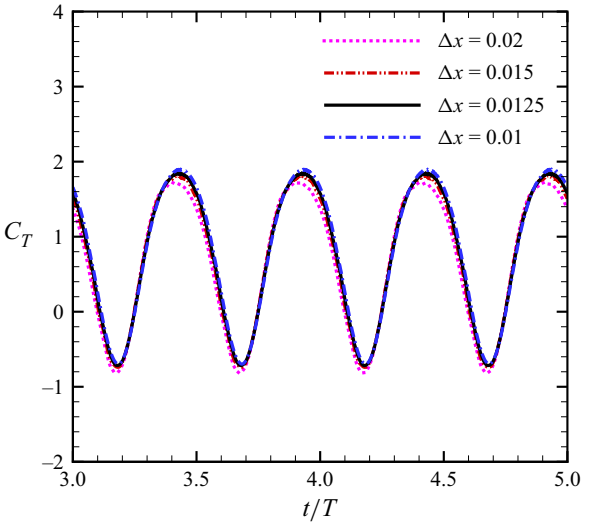

Figure 8. Comparison of the time-dependent thrust coefficient for the four meshes listed in table 3.

each mesh is listed on table 3. Figure 8 shows the time-dependent thrust coefficient with four meshes for Case 1 in table 1, and we observe that the thrust coefficient is converged with the decrease of minimum spacing. The time step is chosen to keep the Courant–Friedrichs–Lewy number at 0.5.

The maximum discrepancy of the time-averaged C_T for M_3 from that for M_4 is within 2 %, and it is confirmed that the numerical result is independent of the mesh spacing and computational domain. Thus, we simulate the present result on mesh M_3 with minimum spacing $\Delta x = 0.0125$ to balance the computational cost and spatial resolution.

Appendix B. Vortex-ring model

A spoon-like vortex surface can be simplified as a vortex ring with the circulation Γ, radius a and inclination angle β to estimate forces, as shown in figure 4(c). The geometry of the simplified vortex ring is determined by the spanwise vorticity on the spanwise symmetry plane $y = 0$.

Considering a particular discrete vortex surface V_i at its shedding time, the centres of two projected regions of the ring on $y = 0$ are

$$\boldsymbol{x}_{c1} = \frac{\int_S \omega_y \boldsymbol{x}\, \mathrm{d}S}{\int_S \omega_y\, \mathrm{d}S} \quad \text{for } \omega_y < 0, \tag{B1}$$

Case	a	β (deg.)	Γ
1	0.530	62.84	1.093
2	0.514	73.09	1.738
3	0.531	69.76	0.961
4	0.591	57.05	1.027

Table 4. Parameters of the vortex-ring model.

and

$$\boldsymbol{x}_{c2} = \frac{\int_S \omega_y \boldsymbol{x}\,\mathrm{d}S}{\int_S \omega_y\,\mathrm{d}S} \quad \text{for } \omega_y > 0. \tag{B2}$$

Then, a and β are obtained by $\boldsymbol{x}_{c1}$ and $\boldsymbol{x}_{c2}$, and

$$\Gamma = \int_S \omega_y\,\mathrm{d}S \tag{B3}$$

is calculated in the region S with $\omega_y > 0$. The parameters a, β and Γ in the present DNS cases are listed in table 4. The time-averaged thrust coefficient

$$\bar{C}_T^R = \frac{I_x}{\frac{1}{2}\rho U^2 R_A T_f c^2} = \frac{2\pi a^2 \Gamma \cos\beta}{U^2 R_A T_f c^2} \tag{B4}$$

is calculated and listed in table 2.

Appendix C. Estimating thrust from the wake with complex vortex topology

The wake is composed of a series of discrete vortex surfaces in Cases 1–4 (see table 1), whereas it becomes convoluted with an increase of the Reynolds number, Strouhal number or plate aspect ratio. As shown in figure 9(*a*), vortex surfaces in the wake become partially interconnected in Case 5 with $R_A = 2$.

The shedding mechanism of vortex surfaces in Case 5 is similar to that in Case 1, but a long, chain-like structure is formed in the wake for $R_A = 2$ instead of the discrete wake structures for $R_A = 1$, hindering the estimation of thrust based on a finite-sized vortex surface. Moreover, we reduce the empirical parameter as $\alpha_l = 1$ in (2.15) in the VSF calculation of Case 5, because the VSF numerical dissipation grows with the complexity of wake structures.

In Case 5, adjacent vortex surfaces can be partially overlapping, and are not easy to separate. Figure 9(*b*) shows the contour of spanwise vorticity and typical VSF isocontour lines on the spanwise symmetry plane at $y = 0$. The extracted VSF isosurface is interconnected for small ϕ_v, e.g. $\phi_v = 0.2$ in figure 9(*b*), and it gradually becomes discrete with increasing ϕ_v, e.g. for $\phi_v = 0.8$.

For an isolated vortex surface, we define the vortical impulse

$$I_x^s(C_\phi) = \boldsymbol{e}_x \cdot \tfrac{1}{2} \int_{V(\phi_v \le C_\phi)} \boldsymbol{x} \times \rho\boldsymbol{\omega}\,\mathrm{d}V \tag{C1}$$

over the volume $V(\phi_v \ge C_\phi)$ filled with VSF isosurfaces of $\phi_v \ge C_\phi$, where $0 \le C_\phi \le 1$ is a constant and $\boldsymbol{e}_x$ denotes the unit vector in the x-direction. In general, $I_x^s(C_\phi)$ and $V(\phi_v \le C_\phi)$ increase with the decrease of C_ϕ.

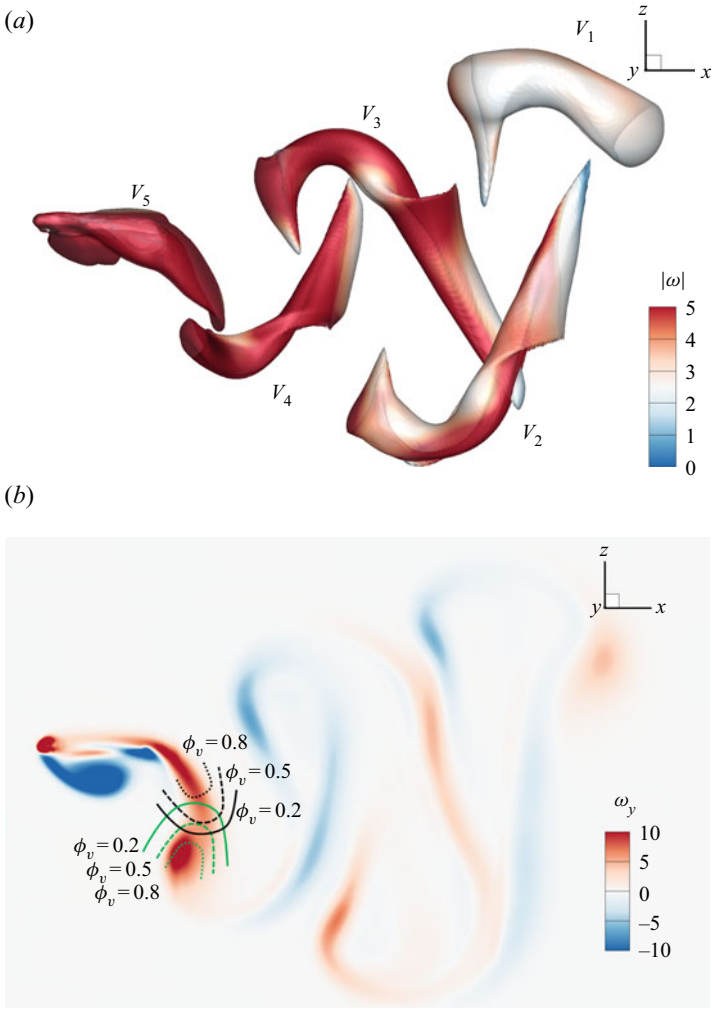

Figure 9. (*a*) The side view of the VSF isosurface of $\phi_v = 0.8$ at $t = 2.25T$ in Case 5. (*b*) The contour of the spanwise vorticity on the spanwise symmetry plane at $y = 0$. Green and black lines represent parts of typical VSF isocontour lines of $\phi_v = 0.2$ (solid), $\phi_v = 0.5$ (dashed) and $\phi_v = 0.8$ (dotted) in V_4 and V_5, respectively.

We estimate $I_x^s = I_x^s(C_\phi = 0)$ in (4.25) from $I_x^s(C_\phi)$ of isolated vortex surfaces, where C_ϕ should be large enough, e.g. $C_\phi = 0.8$. For Case 5, we find a linear relation of $I_x^s(C_\phi)$ with C_ϕ for $C_\phi < 0.8$ as

$$I_x^s(C_\phi) = I_x^s(C_\phi = 0.8) + (0.8 - C_\phi)k_d, \tag{C2}$$

where $k_d \approx 1.02$ is the decay rate of $I_x^s(C_\phi)$ with C_ϕ. Thus, we approximate I_x^s via (C2) with $C_\phi = 0$ at $t = 2.25T$. Then we estimate $\bar{C}_T$ from near wake, which has $\varepsilon \approx 20\,\%$. Therefore, we provide a possible method to estimate thrust from a wake consisting of partially interconnected vortex surfaces.

For larger St or R_A with more convoluted vortex surfaces in the wake, we cannot simply divide the VSF isosurface into discrete ones using the segmentation algorithm with any choice of ϕ_v, e.g. in Case 6. Hence, it is difficult to estimate thrust from an isolated vortex surface in the wake via the simplified thrust formula (4.25), and we have to consider all

the interconnected vortex surfaces near the plate. We find that the thrust can be estimated by (4.13) with an appropriate Σ_b and the relative error is approximately 12 % for Case 6. Therefore, estimating forces based on vortex surfaces in complex wake flows remains an open problem.

References

Bhat, S.S., Zhao, J., Sheridan, J., Hourigan, K. & Thompson, M.C. 2020 Effects of flapping-motion profiles on insect-wing aerodynamics. *J. Fluid Mech.* **884**, A8.

Birch, J.M. & Dickinson, M.H. 2003 The influence of wing-wake interactions on the production of aerodynamic forces in flapping flight. *J. Expl Biol.* **206**, 2257–2272.

Blondeaux, P., Fornarelli, F., Guglielmini, L., Triantafyllou, M.S. & Verzicco, R. 2005 Numerical experiments on flapping foils mimicking fish-like locomotion. *Phys. Fluids* **17**, 113601.

Buchholz, J.H.J. & Smits, A.J. 2006 On the evolution of the wake structure produced by a low-aspect-ratio pitching panel. *J. Fluid Mech.* **546**, 433–443.

Buchholz, J.H.J. & Smits, A.J. 2008 The wake structure and thrust performance of a rigid low-aspect-ratio pitching panel. *J. Fluid Mech.* **603**, 331–365.

Buchner, A.-J., Honnery, D. & Soria, J. 2017 Stability and three-dimensional evolution of a transitional dynamic stall vortex. *J. Fluid Mech.* **823**, 166–197.

Burgers, J.M. 1920 On the resistance of fluids and vortex motion. *Proc. K. Akad. Wet. Amsterdam* **23**, 774–782.

Chang, C.C. 1992 Potential flow and forces for incompressible viscous flow. *Proc. R. Soc. Lond.* A **437**, 517–525.

Chen, Y., Ryu, J., Liu, Y. & Sung, H.J. 2020 Flapping dynamics of vertically clamped three-dimensional flexible flags in a Poiseuille flow. *Phys. Fluids* **32**, 071905.

Dabiri, J.O. 2005 On the estimation of swimming and flying forces from wake measurements. *J. Expl Biol.* **208**, 3519–3532.

Dabiri, J.O. 2009 Optimal vortex formation as a unifying principle in biological propulsion. *Annu. Rev. Fluid Mech.* **41**, 17–33.

Dong, H., Mittal, R. & Najjar, F.M. 2006 Wake topology and hydrodynamic performance of low-aspect-ratio flapping foils. *J. Fluid Mech.* **566**, 309–343.

Drucker, E.G. & Lauder, G.V. 1999 Locomotor forces on a swimming fish: three-dimensional vortex wake dynamics quantified using digital particle image velocimetry. *J. Expl Biol.* **202**, 2393–2412.

Franke, R. 1982 Scattered data interpolation: tests of some methods. *Math. Comput.* **38**, 181–200.

Gharib, M., Rambod, E. & Shariff, K. 1998 A universal time scale for vortex ring formation. *J. Fluid Mech.* **360**, 121–140.

Hedenström, A., Johansson, L.C., Wolf, M., von Busse, R., Winter, Y. & Spedding, G.R. 2007 Bat flight generates complex aerodynamic tracks. *Science* **316**, 894–897.

Hedenström, A., Rosén, M. & Spedding, G.R. 2006 Vortex wakes generated by robins *Erithacus rubecula* during free flight in a wind tunnel. *J. R. Soc. Interface* **3**, 263–276.

Hubel, T.Y., Riskin, D.K., Swartz, S.M. & Breuer, K.S. 2010 Wake structure and wing kinematics: the flight of the lesser dog-faced fruit bat, *Cynopterus brachyotis*. *J. Expl Biol.* **213**, 3427–3440.

Hunt, J.C.R., Wray, A.A. & Moin, P. 1988 Eddies, streams, and convergence zones in turbulent flows. In *Proceedings of Summer Program 1988*, pp. 193–208. Center for Turbulence Research, Stanford University.

Jeong, J. & Hussain, F. 1995 On the identification of a vortex. *J. Fluid Mech.* **285**, 69–94.

Jiménez, J.M., Hultmark, M. & Smits, A.J. 2010 The intermediate wake of a body of revolution at high Reynolds numbers. *J. Fluid Mech.* **659**, 516–539.

Kang, L.L., Liu, L.Q., Su, W.D. & Wu, J.Z. 2018 Minimum-domain impulse theory for unsteady aerodynamic force. *Phys. Fluids* **30**, 016107.

King, J.T., Kumar, R. & Green, M.A. 2018 Experimental observations of the three-dimensional wake structures and dynamics generated by a rigid, bioinspired pitching panel. *Phys. Rev. Fluids* **3**, 034701.

Lauder, G.V. 2015 Fish locomotion: recent advances and new directions. *Annu. Rev. Mar. Sci.* **7**, 521–545.

Lauder, G.V. & Drucker, E.G. 2002 Forces, fishes, and fluids: hydrodynamic mechanisms of aquatic locomotion. *News Physiol. Sci.* **17**, 235–240.

Lee, J., Park, Y.-J., Jeong, U., Cho, K.-J. & Kim, H.-Y. 2013 Wake and thrust of an angularly reciprocating plate. *J. Fluid Mech.* **720**, 545–557.

Lee, J.-J., Hsieh, C.-T., Chang, C.C. & Chu, C.-C. 2012 Vorticity forces on an impulsively started finite plate. *J. Fluid Mech.* **694**, 464–492.

LI, C. & DONG, H. 2016 Three-dimensional wake topology and propulsive performance of low-aspect-ratio pitching-rolling plates. *Phys. Fluids* **28**, 071901.
LI, C., DONG, H. & LIANG, Z. 2016 Proper orthogonal decomposition analysis of 3-D wake structures in a pitching-rolling plate. *AIAA Paper* 2016-2071.
LI, G.-J. & LU, X.-Y. 2012 Force and power of flapping plates in a fluid. *J. Fluid Mech.* **712**, 598–613.
LIGHTHILL, M.J. 1986 *An Informal Introduction to Theoretical Fluid Mechanics*. Clarendon Press.
LIN, Y.-S., TZENG, Y.-T., HSIEH, C.-T., CHANG, C.C. & CHU, C.-C. 2018 A mechanism of thrust enhancement on a heaving plate due to flexibility at moderately low Reynolds numbers. *J. Fluid Struct.* **76**, 573–591.
LIU, G., DONG, H. & LI, C. 2016 Vortex dynamics and new lift enhancement mechanism of wing-body interaction in insect forward flight. *J. Fluid Mech.* **795**, 634–651.
MENDELSON, L. & TECHET, A.H. 2015 Quantitative wake analysis of a freely swimming fish using 3D synthetic aperture PIV. *Exp. Fluids* **56**, 135.
MÜELLER, U.K., VAN DEN HEUVEL, B.L.E., STAMHUIS, E.J. & VIDELER, J.J. 1997 Fish foot prints: morphology and energetics of the wake behind a continuously swimming mullet (Chelon labrosus Risso). *J. Expl Biol.* **200**, 2893–2906.
NAUEN, J.C. & LAUDER, G.V. 2002 Hydrodynamics of caudal fin locomotion by chub mackerel, *Scomber japonicus* (Scombridae). *J. Expl Biol.* **205**, 1709–1724.
NOCA, F., SHIELS, D. & JEON, D. 1997 Measuring instantaneous fluid dynamic forces on bodies, using only velocity fields and their derivatives. *J. Fluid Struct.* **11**, 345–350.
NOCA, F., SHIELS, D. & JEON, D. 1999 A comparison of methods for evaluating time-dependent fluid dynamic forces on bodies, using only velocity fields and their derivatives. *J. Fluid Struct.* **13**, 551–578.
OH, S., LEE, B., PARK, H., CHOI, H. & KIM, S.-T. 2020 A numerical and theoretical study of the aerodynamic performance of a hovering rhinoceros beetle (*Trypoxylus dichotomus*). *J. Fluid Mech.* **885**, A18.
PARK, H., PARK, Y.-J., LEE, B., CHO, K.-J. & CHOI, H. 2016 Vortical structures around a flexible oscillating panel for maximum thrust in a quiescent fluid. *J. Fluid Struct.* **67**, 241–260.
PARK, S.G., CHANG, C.B., HUANG, W. -X. & SUNG, H.J. 2014 Simulation of swimming oblate jellyfish with a paddling-based locomotion. *J. Fluid Mech.* **748**, 731–755.
PESKIN, C.S. 2002 The immersed boundary method. *Acta Numerica* **11**, 479–517.
PHAN, H.V. & PARK, H.C. 2019 Insect-inspired, tailless, hover-capable flapping-wing robots: recent progress, challenges, and future directions. *Prog. Aerosp. Sci.* **111**, 100573.
PRANDTL, L. 1918 Theory of lifting surface. *Nachr. Ges. Wiss. Göttingen* **1918**, 451–477.
SHYY, W., AONO, H., CHIMAKURTHI, S.K., TRIZILA, P., KANG, C.-K., CESNIK, C.E.S. & LIU, H. 2010 Recent progress in flapping wing aerodynamics and aeroelasticity. *Prog. Aerosp. Sci.* **46**, 284–327.
SPEDDING, G.R., ROSÉN, M. & HEDENSTRÖM, A. 2003 A family of vortex wakes generated by a thrush nightingale in free flight in a wind tunnel over its entire natural range of flight speeds. *J. Expl Biol.* **206**, 2313–2344.
TAIRA, K., BRUNTON, S.L., DAWSON, S.T.M., ROWLEY, C.W., COLONIUS, T., MCKEON, B.J., SCHMIDT, O.T., GORDEYEV, S., THEOFILIS, V. & UKEILEY, L.S. 2017 Modal analysis of fluid flows: an overview. *AIAA J.* **55**, 4013–4041.
TAIRA, K. & COLONIUS, T. 2009 Three-dimensional flows around low-aspect-ratio flat-plate wings at low Reynolds numbers. *J. Fluid Mech.* **623**, 187–207.
TONG, W., YANG, Y. & WANG, S. 2020 Characterizing three-dimensional features of vortex surfaces in the flow past a finite plate. *Phys. Fluids* **32**, 011903.
WANG, C., GAO, Q., WANG, H., WEI, R., LI, T. & WANG, J. 2016 Divergence-free smoothing for volumetric PIV data. *Exp. Fluids* **57**, 15.
WANG, S., HE, G. & LIU, T. 2019 Estimating lift from wake velocity data in flapping flight. *J. Fluid Mech.* **868**, 501–537.
WANG, S., HE, G. & ZHANG, X. 2015 Lift enhancement on spanwise oscillating flat-plates in low-Reynolds-number flows. *Phys. Fluids* **27**, 061901.
WANG, S. & ZHANG, X. 2011 An immersed boundary method based on discrete stream function formulation for two- and three-dimensional incompressible flows. *J. Comput. Phys.* **230**, 3479–3499.
WANG, S., ZHANG, X., HE, G. & LIU, T. 2013 A lift formula applied to low-Reynolds-number unsteady flows. *Phys. Fluids* **25**, 093605.
WANG, X.X. & WU, Z.N. 2010 Stroke-averaged lift forces due to vortex rings and their mutual interactions for a flapping flight model. *J. Fluid Mech.* **654**, 453–472.
WU, J., LIU, L. & LIU, T. 2018 Fundamental theories of aerodynamic force in viscous and compressible complex flows. *Prog. Aerosp. Sci.* **99**, 27–63.

WU, J.C. 1981 Theory for aerodynamic force and moment in viscous flows. *AIAA J.* **19**, 432–441.
WU, J.-Z., LU, X.-Y. & ZHUANG, L.-X. 2007 Integral force acting on a body due to local flow structures. *J. Fluid Mech.* **576**, 265–286.
WU, J.-Z., MA, H.-Y. & ZHOU, M.-D. 2015 *Vortical Flows*. Springer.
WU, T.Y. 2011 Fish swimming and bird/insect flight. *Annu. Rev. Fluid Mech.* **43**, 25–58.
XIONG, S. & YANG, Y. 2017 The boundary-constraint method for constructing vortex-surface fields. *J. Comput. Phys.* **339**, 31–45.
XIONG, S. & YANG, Y. 2019 Identifying the tangle of vortex tubes in homogeneous isotropic turbulence. *J. Fluid Mech.* **874**, 952–978.
YANG, Y. & PULLIN, D.I. 2010 On Lagrangian and vortex-surface fields for flows with Taylor–Green and Kida–Pelz initial conditions. *J. Fluid Mech.* **661**, 446–481.
YANG, Y. & PULLIN, D.I. 2011 Evolution of vortex-surface fields in viscous Taylor–Green and Kida–Pelz flows. *J. Fluid Mech.* **685**, 146–164.
ZHAO, Y., YANG, Y. & CHEN, S. 2016 Vortex reconnection in the late transition in channel flow. *J. Fluid Mech.* **802**, R4.
ZHENG, W., RUAN, S., YANG, Y., HE, L. & CHEN, S. 2019 Image-based modelling of the skin-friction coefficient in compressible boundary-layer transition. *J. Fluid Mech.* **875**, 1175–1203.